IEEE Access
Multidisciplinary | Rapid Review | Open Access Journal

Received June 26, 2019, accepted July 26, 2019, date of publication August 2, 2019, date of current version August 15, 2019.

Digital Object Identifier 10.1109/ACCESS.2019.2932721

Cell Search Techniques for Underwater Acoustic Cellular Systems

MUHAMMAD ASIM[1], ROTHNA PEC[2], TAE HO IM[3], AND YONG SOO CHO[1]

[1]Department of Electrical and Electronics Engineering, Chung-Ang University, Seoul 06974, South Korea
[2]Department of Electrical and Energy Engineering, Institute of Technology of Cambodia, Phnom penh 12000, Cambodia
[3]Department of Oceanic IT Engineering, Hoseo University, Asan-si 336-795, South Korea

Corresponding author: Yong Soo Cho (yscho@cau.ac.kr)

This work was supported by the Ministry of Oceans and Fisheries, South Korea, through the project titled Development of Distributed Underwater Monitoring and Control Networks.

ABSTRACT The concept of frequency reuse has been considered for underwater acoustic cellular (UAC) systems owing to the limited available bandwidth of acoustic channels. In a UAC system, the underwater equipment (UE) should detect the identity of the underwater base station (UBS) and synchronize to a serving UBS. In this paper, two different types of cell search techniques are proposed for the downlink of UAC systems based on orthogonal frequency-division multiplexing (OFDM): a Zadoff–Chu sequence-based cell search technique (ZCS-CST) and a linear frequency modulation-based cell search technique (LFM-CST), all at the physical layer. The performances (correlation property, detection probability, and false alarm probability) of the cell search techniques are analyzed and compared with the simulation results in the additive white Gaussian noise (AWGN) and multipath channels. The performances of the cell search techniques are evaluated using the Bellhop channel simulator and field experiment. It is shown that the ZCS-CST is applicable to UAC systems with a small Doppler shift, while the LFM-CST is suitable for UAC systems with a large Doppler shift.

INDEX TERMS Underwater acoustic cellular system, cell search, synchronization, Doppler shift.

NOMENCLATURE

A. ABBREVIATIONS

UAC:	Underwater acoustic cellular
CID:	Cell identification
UE:	User equipment
LFM:	Linear frequency modulation
ZCS:	Zadoff-Chu sequence
DP:	Detection preamble
CFO:	Carrier frequency offset
SSs:	Synchronization signals
CSTs:	Cell search techniques
OFDM:	Orthogonal frequency division multiplexing
STO:	Symbol time offset
AWGN:	Additive white gaussian noise
LTE:	Long term evaluation
CDMA:	Code division multiple access
FFT:	Fast Fourier transform
AUVs:	Autonomous underwater vehicles
CSS:	Chirp spread spectrum
LOS:	Line of sight
CP:	Cyclic prefix

B. PARAMETERS

DFT	Discrete Fourier transform
TDoA	Time delay of arrival
R_c	Cell radius
f	Carrier frequency
κ	Spreading loss
d_0	Reference distance
$a_{dB/km(f)}$	Absorption coefficient
$w(t)$	Additive white gaussian noise
$h_{b,l}(t)$	Time varying channel
η_b	Path loss
$\tau_{b,l}$	Propagation loss
$f_{D,b}$	Doppler shift
f_b	Initial or shifting frequency
ω_b	Frequency sweeping parameter
u_b	Root index of ZCS
N_{ZC}	Length of ZCS
T	Symbol duration excluding CP
T_{CP}	Cyclic prefix duration
ϵ	CFO / Normalized Doppler shift
δ	Symbol time offset
$R_b^{ZC}(\delta, \epsilon)$	Ambiguity function of ZCS

The associate editor coordinating the review of this manuscript and approving it for publication was Guangjie Han.

$R_{b,c}^{ZC}(\delta, \epsilon)$	Cross-correlation of ZCS
$R_{b}^{LFM}(t, f_D)$	Auto-correlation of LFM
$R_{b,c}^{LFM}(t, f_D)$	cross-correlation function of LFM
N	DFT size
T_{LFM}	Symbol duration of LFM
W	Channel bandwidth
$P_{FA,t}$	False alarm probability
$P_{D,t}$	Detection probability
σ_N^2	Noise variance
I_0	Bessel function of first kind
$Q_1(a, b)$	First order Marcum function
γ	Threshold
B	Number of cell IDs or UBSs
$\hat{C}$	Combination operation

I. INTRODUCTION

Owing to the growing demand of underwater data traffic, interest in the study of underwater communication systems for ocean observation has increased. For example, autonomous underwater vehicles (AUVs) or sea gliders may be deployed in the ocean to collect data, such as real-time videos, environmental data, and security data, for a long period of time [1]–[7]. Although electromagnetic wave is widely used in terrestrial communication systems, it is not practical for underwater applications because of severe attenuation caused by the conductive nature of sea water. The acoustic wave is more suitable for an underwater channel because it can propagate for a longer distance. The slow propagation speed of the acoustic wave through sea water is an important factor that differentiates itself from electromagnetic propagation. The slow speed of the acoustic wave combined with multipath trajectories causes a large channel delay spread, while the temporal-variability of the ocean induces significant Doppler shifts. Thus, the underwater acoustic channel is affected by a time and/or frequency dispersion [8]–[10].

Orthogonal frequency division multiplexing (OFDM) system has been considered for underwater acoustic channels because it can cope with the frequency-selective fading caused by a long multipath propagation using a simple equalizer [11]–[13]. Various channel estimation techniques have been developed for OFDM-based underwater acoustic communication because the significant Doppler effects caused by internal waves, platform and sea-surface motion destroy the orthogonality of the sub-carriers and lead to intercarrier interferences [14]–[17]. Also, many different synchronization techniques such as preamble detection, time and frequency synchronization, and Doppler scale estimation/compensation have been developed for OFDM-based underwater acoustic communication [18]–[21]. However, most of these techniques are developed for point-to-point or point-to-multipoint communication in a single cell (not multi-cell environment).

The concept of frequency reuse has been considered for underwater acoustic systems to increase its coverage and capacity because the available bandwidth for an underwater acoustic channel is limited to the low frequency region and strongly depends upon the transmission range and frequency [22]. It was shown that an underwater acoustic cellular (UAC) system based on OFDM can achieve a higher capacity than that of a single carrier system [23]. A code-division multiple access (CDMA)-based UAC system, cellular underwater wireless optical CDMA system, and multiple architectural layer were proposed in [24]–[26].

Like terrestrial cellular systems, the underwater equipment/nodes (UEs) in a UAC system should establish a communication link with an underwater base station (UBS) during the initial synchronization and cell search period, using downlink synchronization signals. The initial synchronization in the UAC system may include signal detection, timing acquisition, frequency acquisition, and Doppler scale estimation. The cell search involves the estimation of the physical cell identity (cell ID) of the UBS. The downlink synchronization signals suitable for UAC systems should be transmitted from the UBSs so that UEs can acquire the synchronization parameters and cell ID (CID) of the serving UBS. After completing synchronization and cell identification, the UE will be able to demodulate the downlink signals, including the broadcast and dedicated information, and to perform a random-access procedure, establishing a communication link between the UE and UBS [27]–[29]. In this study, we focus on the design of the downlink synchronization signals suitable for UAC systems.

Cell search techniques have been developed mainly for radio-based terrestrial cellular systems using downlink synchronization signals. The cell searching techniques developed for terrestrial cellular systems may be considered for the design of the downlink preamble and cell search algorithm for the UAC system. However, the large discrepancy of the propagation speed between the radio wave and acoustic wave may affect the performance of the cell search technique. Because the slow propagation speed of the acoustic wave introduces a large Doppler spread or shift, the radio-based technique may perform differently in the UAC system. In this study, the downlink synchronization signals suitable for UAC systems are proposed so that the UE can estimate the synchronization parameters and cell ID of the serving UBS. After describing the downlink frame structure and synchronization techniques suitable for UAC systems, we propose two different cell search techniques (CSTs).

The first CST can be viewed as a modified version of a CST used in LTE systems, as both techniques are based on the Zadoff-Chu sequence (ZCS). In the ZCS-based CST (ZCS-CST), the cell ID is mapped to the root index of the ZCS, and the cell ID is estimated from the synchronization signal generated by the ZCS. In the ZCS-CST, the cell ID estimation is performed after completing signal detection and synchronization. The second CST is based on a linear frequency modulation (LFM) waveform. Although the LFM signals have been widely used for surveillance applications such as radar and sonar because of their robustness

to Doppler shift, it has not been used for preamble design in cellular networks. In radar and sonar systems, the transmitted signal is correlated with the received echo signal to estimate the parameters such as range, angle, and velocity. In these systems, there is no need to carry the information of the transmitter identity in the transmitted signal. However, in cellular networks, a large number of different preambles need to be generated so that the mobile station can distinguish the preambles transmitted from different base stations. In the proposed LFM-based CST (LFM-CST), the CID is estimated from the LFM waveform, where the CID is mapped to its frequency sweeping and shifting parameters. In the LFM-CST, signal detection and cell identification are performed jointly before synchronization. The performances of the proposed techniques are investigated by analyzing their detection and false alarm probabilities in the AWGN and multipath channels. The performances of the proposed techniques are also evaluated using the Bellhop channel simulator widely used for underwater acoustic communications. Also, as a part of research project for the development of a UAC system, field experiment is performed to verify the correlation properties and detection probability of the cell search techniques derived in this paper. Based on the simulation, the LFM-CST is suitable for the UAC systems with a large Doppler shift because the LFM waveform is a Doppler-insensitive waveform. The experimental results confirm that the ZCS-CST is still applicable to the UAC systems, where a Doppler shift is not significant.

The contributions of this paper can be summarized as follows:

- Downlink synchronization and cell search techniques for UAC systems are described.
- Two different cell search techniques (ZCS-CST and LFM-CST) are proposed for UAC systems.
- Correlation property, detection probability, and false alarm probability of the cell search techniques are analyzed and compared with the simulation results.
- The performances of the cell search techniques are evaluated using the Bellhop (time-varying multipath) channel simulator and verified by field experiment.

The remainder of this study is organized as follows. In Section II, a system model for the UAC system including the frame structure is described. In Section III, two proposed cell search techniques (ZCS-CST and LFM-CST) for UAC systems are described. Auto- and cross-correlation properties of the two cell search techniques are analyzed and compared with the simulation results when a Doppler shift exists. The detection probability and false alarm probability of the cell search techniques are also derived. In Section IV, the detection probability and false alarm probability of the cell search techniques are evaluated in the AWGN and multipath channels using the Bellhop channel simulator. In Section V, the results on the field experiment are discussed. Conclusions are drawn in Section VI.

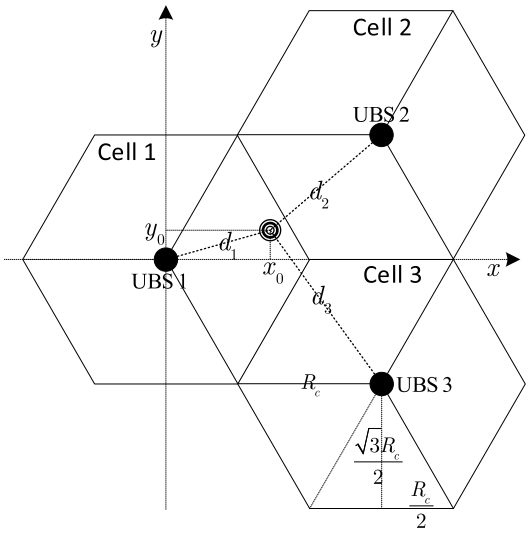

FIGURE 1. Top view of the typical UAC system with 3 UBSs.

II. SYSTEM MODEL

Fig. 1 shows a typical UAC architecture with three hexagonal-shape cells. Here, it is assumed that one UE is located at the boundary of cell 1. The cell radius and carrier frequency in each cell are R_c and f, respectively. The small-scale fading in the underwater acoustic channel is characterized by time-varying and sparse multipath owing to the low speed of the sound wave and propagation in multiple trajectories. The large-scale fading is characterized by the path loss, which depends on the frequency and distance. The path loss of the underwater acoustic wave at distance d from the transmitter is given by [30].

$$\mathrm{PL_{dB}} = 10\kappa \log_{10}\left(\frac{d}{d_0}\right) + (d - d_0)\, a_{\mathrm{dB/km}}(f) \tag{1}$$

Here, κ, d_0 and $a_{\mathrm{dB/km}}(f)$ denote the spreading loss, reference distance, and absorption coefficient given by Throp's formula, respectively, as follows.

$$a_{\mathrm{dB/km}}(f) = \frac{0.11f^2}{1+f^2} + \frac{44f^2}{4100+f^2} + 2.75\times 10^{-4} f^2 + 0.003 \tag{2}$$

The first and second terms in (1) represent the spreading loss and absorption loss, respectively. The spreading loss consists of the cylindrical spreading loss in shallow water and the spherical spreading loss in deep water. The range of κ is between 1 and 2. For a practical system, $\kappa = 1.5$ [30]. The frequency reuse factor is assumed to be one. Exploiting the hexagonal geometry, the distance between the UE and each UBS is given as follows.

$$d = \frac{1}{2}\begin{cases} 2\sqrt{x_0^2 + y_0^2}, & \text{UE-UBS 1} \\ \sqrt{(3R_c - 2x_0)^2 + \left(\sqrt{3}R_c - 2y_0\right)^2}, & \text{UE-UBS 2} \\ \sqrt{(3R_c - 2x_0)^2 + \left(\sqrt{3}R_c + 2y_0\right)^2}, & \text{UE-UBS 3} \end{cases} \tag{3}$$

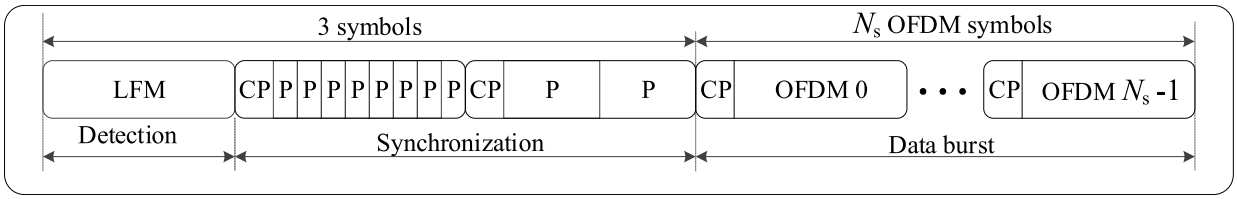

FIGURE 2. Frame structure.

Here, x_0 and y_0 denote the coordinate values of a point where the UE is located. Here, the cell radius R_c and carrier frequency f are set to 5 km and 24.5 kHz, respectively. As shown in Fig. 1, the UBS and UE are located in the 2D $(x-y)$ plane. It is assumed that UBS1 is located at the origin of the coordinate system. If the UE is located at $x_0 = 4.5$ km and $y_0 = 0.15$ km in cell 1, the corresponding distances are 4.5 km for UE-UBS1, 5.14 km for UE-UBS2, and 5.39 km for UE-UBS3. The path losses at these distances are 81.34 dB, 86 dB, and 87.76 dB for UBS1, UBS2, and UBS3, respectively. With a sampling rate of 5 kHz, the time difference of arrival (TDoA) normalized to the earliest arrival path are 0 sample {(4.5025 km/1.5 km)-(4.5025 km/1.5 km)×5 kHz} for UBS1, 2142 samples {(5.1452 km/1.5 km)-(4.5025 km/1.5 km)×5 kHz} for UBS2, and 2964 samples {(5.3918 km/1.5 km)-(4.5025 km/1.5 km)×5 kHz} for UBS3. The large discrepancy in the TDoA owing to the low speed of the sound wave results in an asynchronous system even when all the UBSs are capable of transmitting their signals synchronously. Various inter-cell interference mitigation techniques, such as fractional frequency reuse, soft frequency reuse, and dynamic channel allocation, can be used in the adjacent cells to reduce the interferences in the downlink of the UAC system.

Fig. 2 shows the downlink frame structure used in the UAC system, and Fig. 3 shows the flowcharts required for receiver processing at the UE for the two different CSTs. The frame consists of the detection preamble (DP), synchronization signals (SSs), and OFDM symbols for the data burst [12]. An LFM waveform is used for preamble detection and coarse timing acquisition owing to its insensitivity to Doppler shift. The SSs with 8-repetitive and 2-repetitive patterns are used to acquire the synchronization parameters, such as the coarse carrier frequency offset (CFO), Doppler scale factor, fine CFO, and fine timing. The ZCS is used to generate the SSs owing to its good correlation property and suitability in the OFDM system. Here, ZCS-8 and ZCS-2 denote the SSs with 8-repeatitive and 2-repetitive patterns generated by the ZCS, respectively. ZCS-8 is used to estimate the coarse CFO value, whereas ZCS-2 is used to estimate the Doppler scale factor and fine CFO. The Doppler scaling effect on the received signal is compensated by the resampling process with the estimated Doppler scale factor. After CFO compensation, the channel is estimated by least square (LS) method using pilots interleaved with data symbols. Finally, the transmitted signal is recovered with frequency-domain zero forcing (ZF)

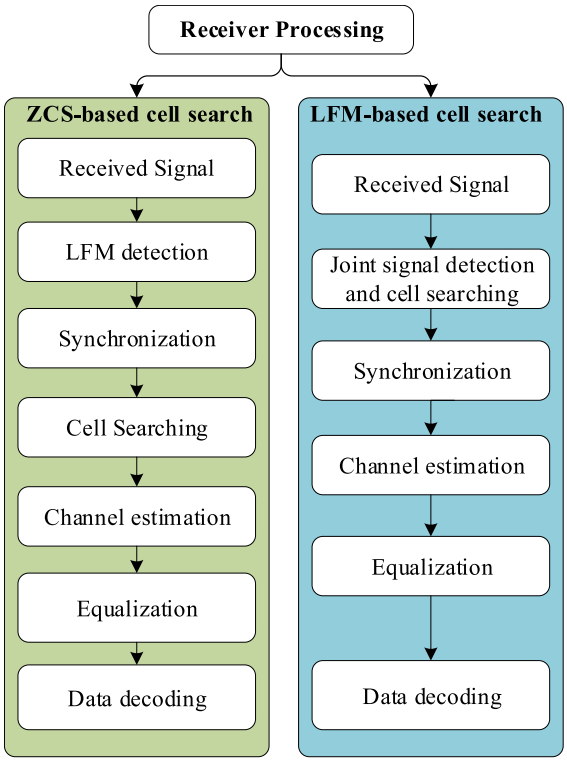

FIGURE 3. Two different synchronization and cell search techniques (ZCS-CST, LFM-CST).

equalizer obtained using the pilots. As shown in Fig. 3, for the ZCS-CST, the preamble detection and synchronization are performed before cell searching. The cell searching is performed using ZCS-2 after synchronization. For the LFM-CST, cell searching is performed jointly with the preamble detection using the received LFM signal. In this study, we focus on the cell search techniques for the UAC system because the synchronization techniques described for underwater acoustic communication systems can be used in the UAC system [11], [20].

Assuming that an underwater channel is sparse with a limited number of multipath components, L, the received signal in a multi-cell environment with B UBSs can be expressed in the continuous-time domain as follows:

$$y(t) = \sum_{b=0}^{B-1} \sum_{l=0}^{L-1} \eta_b h_{b,l}(t)\, x_b\left(t-\tau_{b,l}\right) e^{j2\pi f_{D,b} t} + w(t) \quad (4)$$

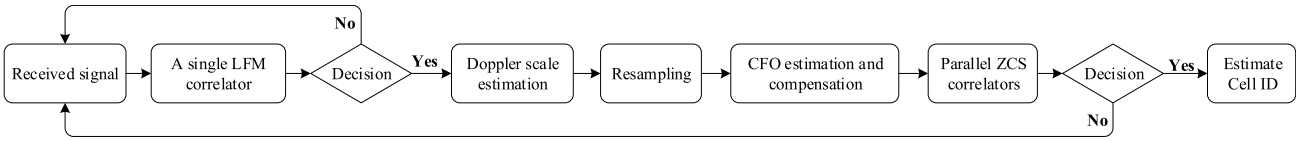

FIGURE 4. ZCS-based cell search technique (ZCS-CST).

where $w(t)$ and $h_{b,l}(t)$ denote an additive white Gaussian noise (AWGN) and time-varying channel coefficient of the l^{th} path for the b^{th} UBS, respectively, both measured at time instant t. Here, $\eta_b \left(= 10^{\mathrm{PL}^b_{\mathrm{dB}}/2}\right)$ denotes the path loss between the UE and b^{th} UBS, which is a function of the distance and frequency. In addition, $x_b(t)$ is the signal transmitted from the b^{th} UBS at time instant t; $\tau_{b,l}$ and $f_{D,b}$ are the propagation delay between the UE and b^{th} UBS for the l^{th} path and the Doppler shift between the UE and b^{th} UBS, respectively. Here, it is assumed that the signals propagating through L paths experience the same amount of Doppler shift.

III. CELL SEARCH TECHNIQUES FOR UAC SYSTEMS

In this section, two different techniques are described for cell searching in UAC systems. It is assumed that the DP and SSs are transmitted periodically or non-periodically in the downlink to facilitate synchronization and cell searching. In the periodical transmission mode, the DP and SSs are transmitted regularly using a similar method to that of the SS transmission in LTE systems. In the non-periodical transmission mode, the DP and SSs are appended to the head of the data packet triggered by the MAC layer, as shown in Fig. 2 The non-periodic transmission can be used in a power saving mode.

A. ZCS-BASED CELL SEARCH TECHNIQUE (ZCS-CST)

As shown in Fig. 4, the received signal in the ZCS-CST is first correlated with a locally-generated LFM signal to perform preamble detection and coarse-timing acquisition. A preamble detection is declared if the output of the LFM correlator is larger than a predefined threshold value. With the reference timing obtained by preamble detection, Doppler scale estimation and fine timing acquisition are performed using the received ZCS-2. Then, the signals in the subsequent frames are resampled using the Doppler scale factor estimated from the first frame. Resampling can be performed in the passband or baseband. However, the residual CFO generated in baseband resampling should be compensated in the later stage, whereas no residual CFO is generated in passband resampling. Then, the CFO is compensated with the coarse and fine CFO values, estimated by the resampled ZCS-8 and ZCS-2. Finally, the ZCS-2 signal after CFO compensation is correlated with a bank of locally-generated ZCSs for CID estimation. A CID is detected when the output of the corresponding ZCS correlator is the largest among the outputs of the parallel ZCS correlators and exceeds a threshold value.

An LFM waveform with a symbol duration T_{LFM}, used for the DP, is generated as follows [11]:

$$x^{\mathrm{LFM}}(t) = x_{T_{\mathrm{LFM}}}(f_0, \omega, t)\, p_{T_{\mathrm{LFM}}}(t) \tag{5}$$

where

$$x_{T_{\mathrm{LFM}}}(f_0, \omega, t) = e^{j\frac{\pi}{T_{\mathrm{LFM}}}\left(2f_0 T_{\mathrm{LFM}} + \omega t^2\right)},$$

$$p_{T_{\mathrm{LFM}}}(t) = \begin{cases} 1, & 0 \le t \le T_{\mathrm{LFM}} \\ 0, & \text{otherwise} \end{cases}$$

Here, ω and f_0 denote the frequency sweeping parameter and initial frequency, respectively. The LFM waveform is widely used for surveillance applications because it is insensitive to the Doppler shift. If the LFM waveform is used for the DP, the target is more likely to be detected even in high Doppler environments. The LFM waveform can produce a significant peak at the output of the LFM correlator for a broad range of Doppler shift. The position of the peak is normally used for coarse timing, which will be used as the reference timing for the acquisition of subsequent SSs. However, its peak will be shifted by the amount proportional to the Doppler shift owing to the property of the LFM waveform. Here, we will investigate the effect of the symbol timing offset (STO) and CFO on the subsequent SS (ZCS-2).

The ZCS is often used for the design of the preamble, synchronization signal, and reference signal in OFDM-based communication systems because it provides an ideal autocorrelation and good cross-correlation properties for complex signals. ZCS-2 carrying CID u_b of the b^{th} UBS is generated in the continuous time-domain as follows:

$$x^{\mathrm{ZC}}_{u_b}(t) = \frac{1}{N_{\mathrm{ZC}}} \sum_{k=0}^{N_{\mathrm{ZC}}-1} Z^{\mathrm{ZC}}_{u_b}(k)\, e^{j\frac{2\pi}{T}k(t-T_{\mathrm{CP}})p_{T_{\mathrm{OFDM}}}(t)}$$
$$k = 0, 1, \ldots\ldots, N_{\mathrm{ZC}} - 1 \tag{6}$$

where N_{ZC} and $T_{\mathrm{OFDM}} = (T + T_{\mathrm{CP}})$ denote the length of the ZCS and overall OFDM symbol duration including the symbol duration T and cyclic prefix (CP) interval T_{CP}, respectively. The frequency-domain ZCS $Z^{\mathrm{ZC}}_{u_b}(k)$ in (6) can be expressed in terms of the time-domain ZCS as follows: [31]

$$Z^{\mathrm{ZC}}_{u_b}(k) = Z^{\mathrm{ZC}}_{u_b}(0)\left(Z^{\mathrm{ZC}}_{u_b}\left(u_b^{-1}k\right)\right)^* \tag{7}$$

where

$$Z^{\mathrm{ZC}}_{u_b}(n) = e^{j\frac{\pi u_b}{N_{\mathrm{ZC}}}n(n+1)} \tag{8}$$

$$Z^{\mathrm{ZC}}_{u_b}(0) = \sum_{n=0}^{N_{ZC}-1} Z^{\mathrm{ZC}}_{u_b}(n) \tag{9}$$

Here u_b^{-1} denotes the multiplicative inverse of u_b. The constant term, $Z^{\mathrm{ZC}}_{u_b}(0)$, can be given in a closed-form using the Gauss sum expression [32]. By sampling (6) at the rate

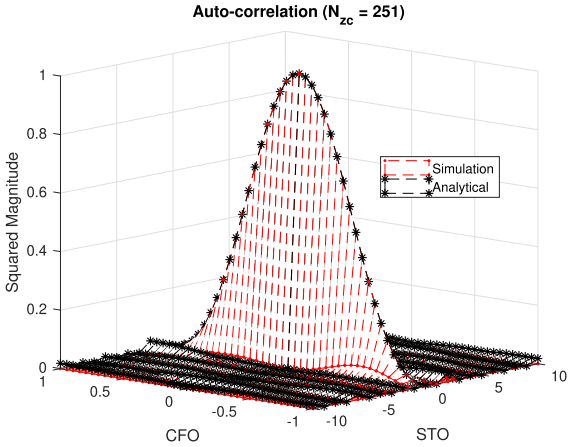

FIGURE 5. Auto-correlation of ZCS-2 in the presence of the STO and CFO.

of $2N_{\mathrm{ZC}}/T$ Hz, (6) can be expressed in the discrete time domain as $x_b{}^{\mathrm{ZC}}(n)$. From (8) one can see that two identical blocks (each with N_{ZC} samples) are produced owing to the periodicity in ZCS, i.e., $Z_{u_b}^{\mathrm{ZC}}(n) = Z_{u_b}^{\mathrm{ZC}}(n+N_{\mathrm{ZC}})$ for $n = 0, 1, \cdots, N_{\mathrm{ZC}}-1$. The linear convolution can be converted into circular convolution using the CP.

An ambiguity function is widely used for waveform design and analysis because it succinctly characterizes the behavior of a waveform paired with its matched filter. The ambiguity function is useful for examining the resolution, sidelobe behavior, and ambiguities in the delay (time shift) and Doppler for a given waveform. Here, a discrete-time version of the ambiguity function of ZCS-2 is investigated to analyze the auto-correlation property of ZCS-2 in the presence of the Doppler shift (normalized CFO: ϵ) as well as the STO (coarse timing error: δ). The discrete-time version of the ambiguity function of ZCS-2 can be obtained as follows.

$$\begin{aligned} R_b^{\mathrm{ZC}}(\delta,\epsilon) &= \frac{1}{N}\sum_{n=0}^{N-1} x_b^{\mathrm{ZC}}(n-\delta)\left(x_b^{\mathrm{ZC}}(n)\right)^* e^{j\frac{2\pi}{N}\epsilon n} \\ &= \frac{Z_{u_b}^{\mathrm{ZC}}(\delta)\, sin\left(\pi\left(\epsilon-2u_b\delta\right)\right)}{N sin\left(\frac{\pi}{N}\left(\epsilon-2u_b\delta\right)\right)} e^{j\frac{\pi}{N}(N-1)(\epsilon-2u_b\delta)} \end{aligned} \tag{10}$$

Here, (10) is obtained using the following property of ZCS.

$$\begin{aligned} Z_{u_b}^{\mathrm{ZC}}(n-\delta) &= e^{j\frac{\pi u_b}{N_{\mathrm{ZC}}}(n-\delta)(n-\delta+1)} \\ &= e^{j\frac{\pi u_b}{N_{\mathrm{ZC}}}n(n+1)} e^{-j\frac{\pi u_b}{N_{\mathrm{ZC}}}\delta(-\delta+1)} e^{-j\frac{\pi u_b\delta}{N_{\mathrm{ZC}}}n} \\ &= Z_{u_b}^{\mathrm{ZC}}(n)\, Z_{u_b}^{\mathrm{ZC}}(-\delta)\, e^{-j\frac{\pi u_b\delta}{N_{\mathrm{ZC}}}n} \end{aligned}$$

Because the range of the normalized CFO ϵ is smaller than the DFT size N, the magnitude of the auto-correlation in (10) at the correct timing can be approximated as $|R_{u_b}^{\mathrm{ZC}}(0,\epsilon)| \approx sinc(\epsilon)$. Thus, even at the correct timing, the magnitude decreases with an increase in the Doppler shift.

The residual CFO and STO are unavoidable for CID estimation in the ZCS-CST because perfect synchronization is not guaranteed. Fig. 5 shows the auto-correlation of ZCS-2, given in (10) in the presence of the Doppler shift as well as the timing error when $N_{\mathrm{ZC}} = 251$ and $u_b = 17$. From this figure, it can be seen that the analytical result agrees well with the simulation result. The magnitude of auto-correlation decreases significantly even with a small timing error, implying that the CID cannot be detected.The magnitude is one at the origin when $(\delta,\epsilon) = (0,0)$ and decreases with an increase in the normalized CFO ϵ. The magnitude becomes zero when the value of the normalized CFO approaches ±1,i.e., $(\delta,\epsilon) = (0,\pm1)$.

A cross-correlation of ZCS-2 in the presence of the STO and CFO can be obtained similarly as follows. The closed-form expression of (11) cannot be obtained for an arbitrary value of the CFO. However, it can be given in the form of the Gauss sum expression when the CFO value is an integer. Consequently, it can be shown that if the sequence length is a prime number, the magnitude of the cross-correlation is a small constant and independent of the STO and CFO.

$$\begin{aligned} R_{b,c}^{\mathrm{ZC}}(\delta,\epsilon) &= \frac{1}{N}\sum_{n=0}^{N-1} x_b^{\mathrm{ZC}}(n-\delta)\left(x_c^{\mathrm{ZC}}(n)\right)^* e^{j\frac{2\pi}{N}\epsilon n} \\ &= \frac{Z_{u_b}^{\mathrm{ZC}}(\delta)}{N}\sum_{n=0}^{N-1} z_{u_b}^{\mathrm{ZC}}(n)\left(x_{u_c}^{\mathrm{ZC}}(n)\right)^* e^{j\frac{2\pi(\epsilon-2u_b\delta)}{N}n} \end{aligned} \tag{11}$$

$$|R_{u_b}^{\mathrm{ZC}}(\delta,\epsilon)| \approx \frac{2\sqrt{N_{\mathrm{ZC}}}}{N} = \frac{1}{\sqrt{N_{\mathrm{ZC}}}} \tag{12}$$

From the result given in (12), it can be seen that the misdetection (incorrect CID estimation) probability is not high even in the presence of the STO and CFO. However, the detection (correct CID estimation) probability is low when there is a synchronization error, as shown in (10).

B. LFM-BASED CELL SEARCH TECHNIQUE (LFM-CST)

In the LFM-CST, cell searching is performed jointly with the preamble detection using the received LFM signal. In order to facilitate the CID estimation from the received LFM signal (at sensor node), multiple LFM preambles are generated in the LFM-CST with the parameters corresponding to its CID (at UBS). The CID b of the b^{th} UBS is mapped to the parameters of the LFM preamble: the starting frequency f_b, and frequency sweeping parameter ω_b. The LFM preamble of the b^{th} UBS is generated in the continuous-time domain as follows:

$$\begin{aligned} x_b^{\mathrm{LFM}}(t) &= x_{T_{\mathrm{LFM}}}(f_b,\omega_b,t)\, p_{T_{\mathrm{LFM}}}(t) \\ &\quad -W \le \omega_b \le W,\ \frac{-W+|\omega_b|}{2} \le f_b \le \frac{W-|\omega_b|}{2} \end{aligned} \tag{13}$$

where

$$x_{T_{\mathrm{LFM}}}(f_b,\omega_b,t) = e^{j\frac{\pi}{T_{\mathrm{LFM}}}\left(2f_bT_{\mathrm{LFM}}t+\omega_bt^2\right)}$$

$$p_{T_{\mathrm{LFM}}}(t) = \begin{cases} 1 & 0 \le t \le T_{\mathrm{LFM}} \\ 0 & \text{otherwise} \end{cases}$$

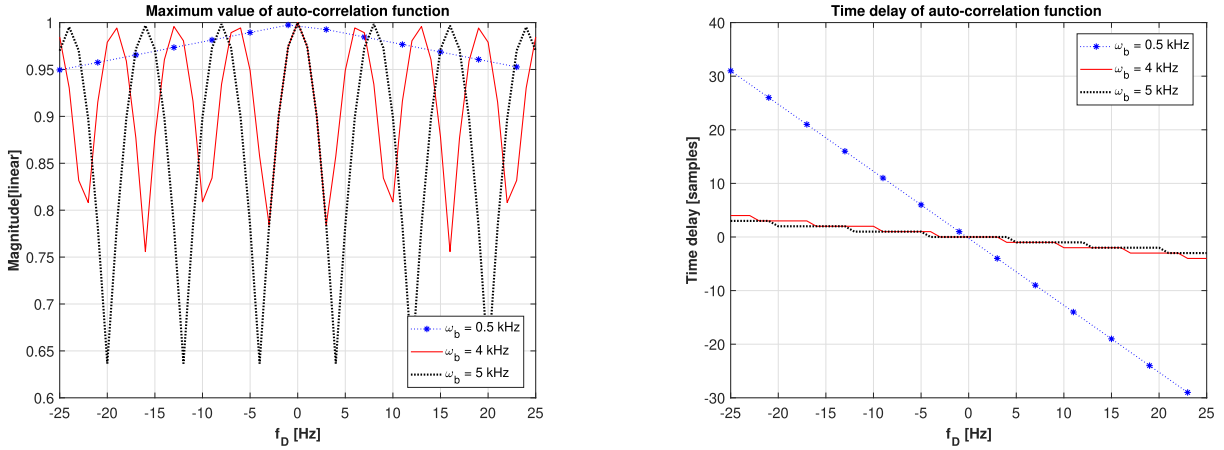

(a) Maximum magnitude vs. f_D **(b)** Time delay vs. f_D

FIGURE 6. Auto-correlation function of the LFM preamble in the LFM-CST.

In (13), T_{LFM} and W denote the LFM symbol duration and operational channel bandwidth, respectively. The LFM preamble carrying the CID information is used for preamble detection and CID estimation. The auto-correlation property of the LFM preamble in the presence of the Doppler shift and time delay can be obtained by

$$\begin{aligned} R_b^{\text{LFM}}(t, f_D) &= \frac{1}{T_{\text{LFM}}} \int_{-\infty}^{+\infty} x_b^{\text{LFM}}(s-t) \left(x_b^{\text{LFM}}(t)\right)^* \\ &\quad \times e^{j2\pi f_D s} ds \\ &= e^{j\pi (f_D (T_{\text{LFM}}+t)+(2f_b+\omega_b)t)} \\ &\quad \times \rho_{\text{LFM}}(t)\, sinc\left(f_D T_{\text{LFM}} + \omega t\right) \end{aligned} \tag{14}$$

where $\rho_{\text{LFM}}(t) = 1 - \frac{|t|}{T_{\text{LFM}}}$. From (14), it can be observed that the magnitude of the auto-correlation function of the LFM preamble varies depending on the values of T_{LFM}, f_D and ω_b. However, the parameter f_b does not have an effect on the magnitude of the auto-correlation function. Fig. (6) shows the auto-correlation function of the LFM preamble when f_D varies. Fig. 6(a) and (b) show the maximum value and corresponding time delay of the auto-correlation function, respectively, for three different values of ω_b, i.e., 0.5 kHz, 4 kHz, and 5 kHz. As shown in Fig. 6(a), the maximum value decreases slowly in a triangular manner when $\omega_b = 0.5$ kHz and fluctuates fast when $\omega_b = (4, 5)$ kHz. However, the time delay increases faster when $\omega_b = 0.5$ kHz, compared to the cases of 4 kHz and 5 kHz, as shown in Fig. 6(b). For example, the time delays at the Doppler shift of 20 Hz are 25, 3, and 2 samples when the values of ω_b are 0.5 kHz, 4 kHz, and 5 kHz, respectively. Thus, to obtain a high detection probability with a small timing error, the value of ω_b should be selected such that a high magnitude and small time delay can be achieved at the output of the correlator. Similarly, a cross-correlation function of the LFM preambles with different cell IDs (b and c) in the presence of a time delay and Doppler shift can be obtained as:

$$\begin{aligned} R_{b,c}^{\text{LFM}}(t, f_D) &= \frac{1}{T_{\text{LFM}}} \int_{-\infty}^{+\infty} x_b^{\text{LFM}}(s-t) \\ &\quad \times \left(x_c^{\text{LFM}}(t)\right)^* e^{j2\pi f_D s} ds \\ &= \frac{1}{T_{\text{LFM}}} \times \frac{C_{b,c}(t, f_D)}{a_{b,c} T_{\text{LFM}}} + jsgn(\Delta\omega) \\ &\quad \times \frac{S_{b,c}(t, f_D)}{a_{b,c} T_{\text{LFM}}} \times e^{j\pi\left(2f_c t - \frac{\omega_c}{T_{\text{LFM}}} t^2\right)} \\ &\quad \times e^{-j\pi \Delta\omega T_{\text{LFM}} \left(\frac{\Delta f T_{\text{LFM}} + \omega_c t + f_D T_{\text{LFM}}}{\Delta\omega T_{\text{LFM}}}\right)} \end{aligned} \tag{15}$$

where $0 \le t \le T_{\text{LFM}}$, $\Delta f = f_b - f_c$, $\Delta\omega = \omega_b - \omega_c$, $\Delta\omega \neq 0$ and

$$\begin{aligned} S_{b,c}(t, f_D) &= S\left(a_{b,c} s_0 + b_{b,c}(t, f_D)\right) \\ &\quad + S\left(a_{b,c} s_t + b_{b,c}(t, f_D)\right) \\ C_{b,c}(t, f_D) &= C\left(a_{b,c} s_0 + b_{b,c}(t, f_D)\right) \\ &\quad + C\left(a_{b,c} s_t + b_{b,c}(t, f_D)\right) \\ s_t &= \frac{T_{\text{LFM}}}{2} - |t|, \quad a_{b,c} = \sqrt{\frac{|\Delta\omega|\pi}{T_{\text{LFM}}}} \\ b_{b,c}(t, f_D) &= \left(\frac{\Delta f T_{\text{LFM}} + \omega_c t + f_D T_{\text{LFM}}}{\Delta\omega T_{\text{LFM}}}\right) \sqrt{|\Delta\omega| T_{\text{LFM}} \pi} \end{aligned} \tag{16}$$

Here, $sgn(.)$ represents the signum function with the values of $\{-1,0,1\}$ for negative, zero, and positive values of ω, respectively. Here, Fresnel integrals are used to derive the cross-correlation function. The cosine and sine Fresnel integrals are defined as follows [33].

$$S(t) = \int_0^t \sin\left(\frac{\pi s^2}{2}\right) ds \quad \text{and } \mathrm{C}(t) = \int_0^t \cos\left(\frac{\pi s^2}{2}\right) ds \tag{17}$$

To analyze the cross-correlation function of LFM preambles with different values of f_c, we rewrite (15) by substituting

$\omega_b = \omega_c$ as follows:

$$R_{b,c}^{\mathrm{LFM}}(t, f_D) = e^{j\pi(f_b t - \frac{\omega_b}{T_{\mathrm{LFM}}} t^2)} \int_{-\infty}^{+\infty} e^{j2\pi(\Delta f t + \frac{\omega_b}{T_{\mathrm{LFM}}} f_D)s} ds$$
$$= e^{j\pi(f_b + \Delta f + f_D)t} \times sinc(\Delta f T_{\mathrm{LFM}} + f_D T_{\mathrm{LFM}} + \omega_b) \quad (18)$$

(18) can be seen as a shifted version of sinc function with a peak value and corresponding time shift:

$$\hat{\rho}_{\mathrm{LFM}}^{b,c} = \rho_{\mathrm{LFM}}(t_s^{b,c}) = t_s^{b,c} = \frac{T_{\mathrm{LFM}}}{\omega_b}(\Delta f + f_D) \quad (19)$$

For a fixed value of ω_b, the time shift increases with Δf and f_D. The peak value decreases as the time shift increases. To avoid false detection of CID, the time shift in (19) should be larger than the symbol duration T_{LFM}:

$$|t_s^{b,c}| \geq T_{\mathrm{LFM}} \Rightarrow \frac{t_s^{b,c}}{T_{\mathrm{LFM}}} \geq 1 \quad (20)$$

Using (20), the time shift in (19) can be written as

$$(\Delta f + f_D) \geq |\omega_b| \quad (21)$$

From (13) and (21), we can obtain a lower and upper bound of Δf as follows:

$$\omega_b \leq \Delta f \leq \frac{W - \omega_b}{2}, \quad \omega_b > 0 \quad (22)$$

The lower and upper bound obtained in (22) should be satisfied for all values of ω_b equal to or less than $W/3$.

In Fig. 7(a) and (c), the analytical solutions in (15) and (18) are compared with simulation results when $f_D = 0$ Hz. The analytical solution in (15) is obtained by a numerical evaluation of the Fresnel integral, whereas the simulation results are obtained through direct cross-correlation operation between two LFM preambles. As shown in Fig. 7(a) and (c), the analytical solution is consistent with the simulation result. Fig. 7(a) is obtained when the value of $\Delta\omega$ is 50 Hz, whereas Fig. 7(c) shows the case when $\Delta\omega = 0$ and $\Delta f = 0$. Fig. 7(b) and (d) shows cross-correlation function for different values of ω_b and f_c. Fig. 7(b) shows the cross-correlation function of LFM preambles with different values of ω_c (0.55 kHz, 2 kHz, and -1 kHz) when $\omega_b = 0.5$ kHz and $f_D = 0$ Hz. As shown in Fig. 7(b), the cross-correlation level decreases as $\Delta\omega$ increases. Similarly, the cross-correlation function of LFM preambles with different values of f_c (250 Hz, 500 Hz, and 750 Hz) are plotted in Fig. 7(d) for a fixed value of $\omega_b = 0.5$ kHz. From this figure, it can be seen that there exists one significant side peak other than the desired peak at origin when $f_c = 500$ Hz ($\Delta f = 250$) Hz. Thus, the value of $\Delta\omega$ should be selected to secure a low correlation among the LFM preambles with different CIDs. Also, if the CID is mapped with different value of f, i.e., f_b or f_c, Δf should satisfy condition in (22) to avoid false detection of CID.

Fig. 8 shows the proposed LFM-CST. In this technique, the received signal is correlated with a bank of locally-generated LFM preambles with different parameters (f_b, ω_b, $\Delta\omega$). The LFM preambles are generated with different sets of (f_b, ω_b) corresponding to the cell IDs of the UBSs. Note that the cross-correlation level between two different LFM preambles decreases as their difference ($\Delta\omega$) increases. However, the number of possible cell IDs decreases with an increase of $\Delta\omega$ Therefore, there is a trade-off between the cross-correlation level and number of cell IDs in selecting the value of $\Delta\omega$. As shown in Fig. 8 the cell ID is detected when its correlation output is the largest among the parallel LFM correlators and greater than a predefined threshold value. In the LFM-CST, the correct cell ID is more likely to be detected even in high Doppler environments because the LFM correlator is insensitive to the Doppler shift.

C. DETECTION PROBABILITY OF THE CELL SEARCH TECHNIQUES

In this section, the performance of the cell searching technique is analyzed based on the detection probability and false alarm probability. The received signal can be modeled under two hypotheses as follows.

$$y(t) = \begin{cases} w(t), & H_0 \\ y(t), & H_1 \end{cases} \quad (23)$$

Hypothesis H_0 (null hypothesis) is when the received signal contains only the background noise, whereas hypothesis H_1 is when the received signal contains signals transmitted from the b^{th} UBS and neighboring UBSs plus the background noise.

For the ZCS-CST, timing is acquired when preamble detection occurs at the output of the LFM correlator as follows:

$$\hat{t}_{acq}(t) = \left\{ t : |r^{\mathrm{LFM}}(t)|^2 > \gamma \right\} \quad (24)$$

where

$$r^{\mathrm{LFM}}(t) = \frac{1}{T_{\mathrm{LFM}}} \int_0^{T_{\mathrm{LFM}}} y(s+t) \left(x^{\mathrm{LFM}}(s) \right)^* ds \quad (25)$$

Here, the random variables under H_1 and H_0 are defined as $Z_{1,t} = |r^{\mathrm{LFM}}(t)|^2$ and $Z_{0,t} = |r^{\mathrm{LFM}}(t)|^2$, respectively. The false alarm probability $P_{\mathrm{FA},t}$ and detection probability $P_{\mathrm{D},t}$ at time instant t are defined as follows.

$$P_{\mathrm{FA},t} = Pr\left\{ Z_{0,t} \geq \gamma \right\} = \int_{\gamma}^{\infty} f_{0,t}(z)\, dz \quad (26)$$

$$P_{\mathrm{D},t} = Pr\left\{ Z_{1,t} \geq \gamma \right\} = \int_{\gamma}^{\infty} f_{1,t}(z)\, dz \quad (27)$$

Here, $f_{0,t}(z)$ and $f_{0,t}(z)$ denote the probability density functions of the random variables, $Z_{0,t}$ and $Z_{1,t}$, respectively. Under the AWGN assumption, $f_{0,t}(z)$ becomes time-independent, and (26) can be expressed as

$$P_{\mathrm{FA},t} = 1 - e^{-\frac{\gamma}{\sigma_N^2}} \quad (28)$$

where σ_N^2 denotes the variance of the random variable, $Re\left\{ r^{\mathrm{LFM}}(t) \right\}$ and $Im\left\{ r^{\mathrm{LFM}}(t) \right\}$, under H_0. Under H_1,

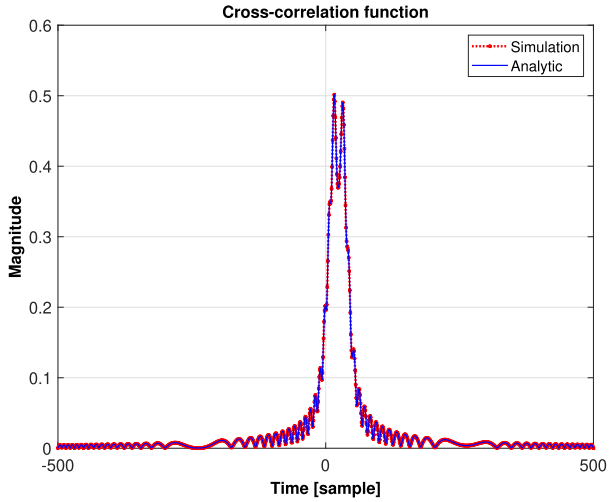

(a) Analytical vs. simulation

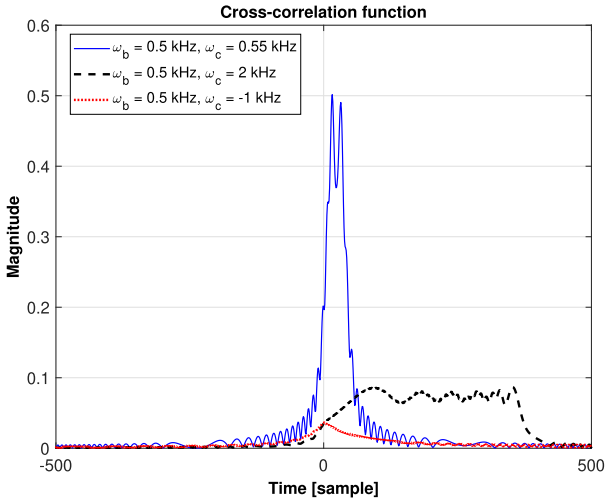

(b) Different values of ω_c

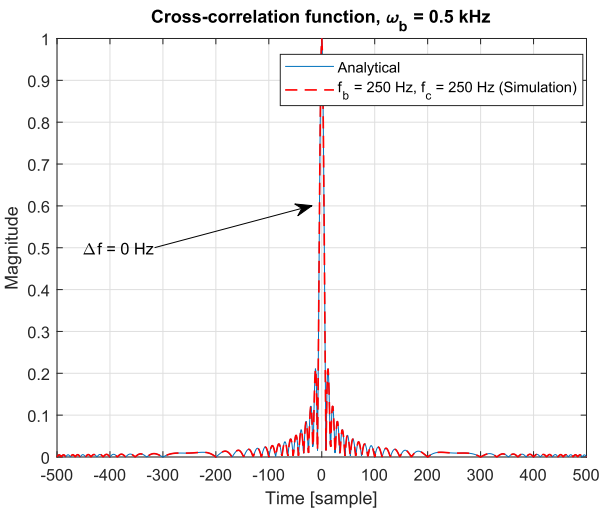

(c) Analytical vs. simulation

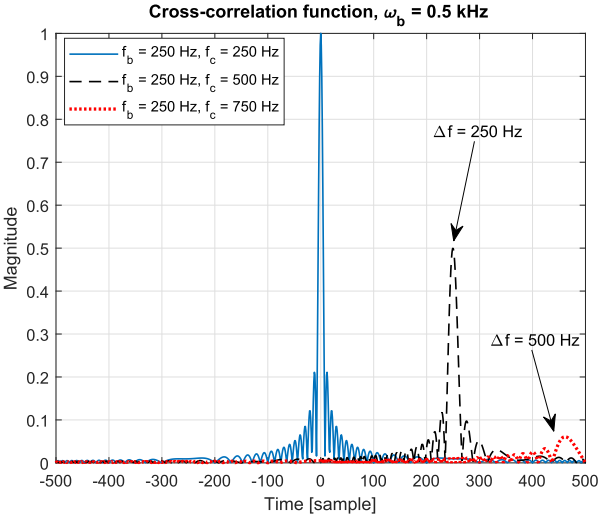

(d) Different values of Δf

FIGURE 7. Cross-correlation function of the LFM preamble in the LFM-CST.

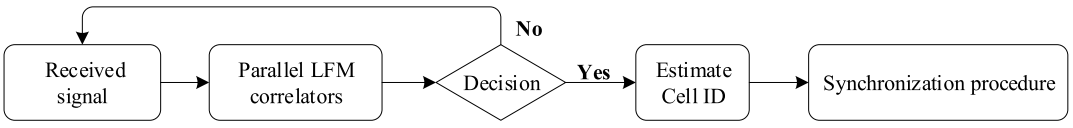

FIGURE 8. LFM-based cell searching technique (LFM-CST).

the cross-correlation function between the received signal and locally-generated LFM preamble is given by

$$r^{\mathrm{LFM}}(t) = \frac{e^{j2\pi f_D t}}{T_{\mathrm{LFM}}}\eta h \int_0^{T_{\mathrm{LFM}}} x^{\mathrm{LFM}}(s+t)\left(x^{\mathrm{LFM}}(s)\right)^* \times e^{j2\pi f_D t} ds + \tilde{w}^{\mathrm{LFM}}(t) \quad (29)$$

where $\tilde{w}^{\mathrm{LFM}}$ denotes the noise term after the cross-correlation with the reference signal (LFM preamble). Here, the channel is assumed to be flat fading. When there is no timing error, (29) is further simplified as follows.

$$r^{\mathrm{LFM}} = \frac{1}{T_{\mathrm{LFM}}}\eta h \int_0^{T_{\mathrm{LFM}}} x^{\mathrm{LFM}}(s)\left(x^{\mathrm{LFM}}(s)\right)^* \times e^{j2\pi f_D t} ds + \tilde{w}^{\mathrm{LFM}} \quad (30)$$

From (30), the output is given by the correlation value of the LFM signal scaled by path loss η and channel coefficient h and added by noise $\tilde{w}^{\mathrm{LFM}}$. The probability density function

corresponding to (30) is given as follows.

$$f_{1,t=0}(z) = \frac{1}{\sigma^2} e^{-\frac{z+\lambda}{\sigma^2}} I_0\left(\frac{2\sqrt{\lambda z}}{\sigma^2}\right) \tag{31}$$

Here, $I_0(z)$ denotes the Bessel function of the first kind of order 0. The parameters are defined as follows.

$$\lambda = \eta^2\left[\left(Re\left\{hR^{\mathrm{LFM}}(t, f_D)\right\}\right)^2 + \left(Im\left\{hR^{\mathrm{LFM}}(t, f_D)\right\}\right)^2\right]$$
$$\sigma^2 = \left(\sigma^{\mathrm{LFM}}\right)^2 \tag{32}$$

Then, the detection probability of the LFM preamble is given as shown below.

$$P^{\mathrm{LFM}}_{\mathrm{D},t=0} = \int_{\gamma}^{\infty} f_{1,t=0}(z)\, dz = Q_1\left(\frac{\sqrt{2\lambda}}{\sigma}, \frac{\sqrt{2\lambda}}{\sigma}\right) \tag{33}$$

In (33), $Q_1(a, b)$ denotes the first-order Marcum function with a and b as the arguments. In the ZCS-CST, a cell ID is detected using ZCS-2 after the preamble detection. If the received signal is not detected by the LFM correlator, the cell search operation will not occur. However, if the preamble is detected, the cell search operation will be performed with parallel ZCS correlators. If the output of the ZCS correlator exceeds a threshold value γ, its cell ID is estimated as follows.

$$\hat{b} = \underset{b}{\mathrm{argmax}} |r^{\mathrm{ZC}}|^2 > \gamma \tag{34}$$

The cross-correlation between the received signal and locally-generated ZCSs for cell ID b is given as follows.

$$\begin{aligned} r^{\mathrm{ZC}} &= \frac{1}{N}\sum_{n=0}^{N-1} y^{\mathrm{ZC}}(n)\left(x^{\mathrm{ZC}}(n)\right)^* \\ &= \frac{1}{N}\sum_{n=0}^{N-1} \eta h x^{\mathrm{ZC}}(n+\delta)\left(x^{\mathrm{ZC}}(n)\right)^* e^{j\frac{2\pi\epsilon}{N}n} + \tilde{w}^{\mathrm{ZC}} \\ &= \eta h R^{\mathrm{ZC}}(\delta, \epsilon) + \tilde{w}^{\mathrm{ZC}} \end{aligned} \tag{35}$$

Here, it is also assumed that the channel is flat fading. When Z_1 is a random variable of $|r^{\mathrm{ZC}}|^2$, the cell ID is detected when Z_1 is the largest among the outputs of the parallel ZCS correlators and exceeds a threshold value γ. The detection probability is given by [34]

$$\begin{aligned} P^{\mathrm{ZC}}_{\mathrm{D},t=0} &= Pr\{Z_1 > Z, Z_1 > \gamma\} \\ &= \int_{\gamma}^{\infty}\left(\int_0^z f_Z(z)\, dz\right)^B f_{Z_1}(z)\, dz \end{aligned} \tag{36}$$

where

$$\begin{aligned} f_Z(z) &= \frac{1}{\left(\sigma^{\mathrm{ZC}}\right)^2} e^{-\frac{z}{\left(\sigma^{\mathrm{ZC}}\right)^2}} \\ f_{Z_1}(z) &= \frac{1}{\left(\sigma^{\mathrm{ZC}}\right)^2} e^{-\frac{z+\lambda^{\mathrm{ZC}}}{\left(\sigma^{\mathrm{ZC}}\right)^2}} I_0\left(\frac{2\sqrt{\lambda^{\mathrm{ZC}} z}}{\left(\sigma^{\mathrm{ZC}}\right)^2}\right) \end{aligned} \tag{37}$$

Here, B denotes the number of cell IDs. Substituting $f_Z(z)$ and $f_{Z_1}(z)$ into (36), the detection probability of the correct cell ID is obtained as follows [35]:

$$P^{\mathrm{ZC}}_{\mathrm{D},t=0} = \frac{1}{2} Q_1\left(\frac{\sqrt{\lambda^{\mathrm{ZC}}}}{\sigma^{\mathrm{ZC}}}, \frac{2\sqrt{\gamma}}{\sigma^{\mathrm{ZC}}}\right) e^{\frac{\lambda^{\mathrm{ZC}}}{2\left(\sigma^{\mathrm{ZC}}\right)^2}} \sum_{i=0}^{B} (-1)^i \hat{C}_i^B \tag{38}$$

where $\hat{C}$ denotes the combination operation. The non-centric parameter, λ^{ZC}, is given as follows.

$$\lambda^{\mathrm{ZC}} = \eta^2\left[\left(Re\left\{hR^{\mathrm{ZC}}(\delta, \epsilon)\right\}\right)^2 + \left(Im\left\{hR^{\mathrm{ZC}}(\delta, \epsilon)\right\}\right)^2\right] \tag{39}$$

In the ZCS-CST, the overall detection probability is given by multiplying (33) and (38) because the cell search operation is performed when the DP is successfully detected. By multiplying the DP detection probability and CID detection probability, the overall detection probability in the ZCS-CST is obtained as follows.

$$P_{\mathrm{D},t=0} = P^{\mathrm{LFM}}_{\mathrm{D},t=0} \times P^{\mathrm{ZC}}_{\mathrm{D},t=0} \tag{40}$$

In addition, the overall false alarm probability in the ZCS-CST is obtained as shown below.

$$P^{\mathrm{ZC}}_{\mathrm{FA}} = 1 - P_{\mathrm{D},t=0} \tag{41}$$

In the LFM-CST, the preamble detection and cell ID detection are performed jointly using parallel LFM correlators. In this technique, a bank of matched filters is used to correlate the received signal with the locally-generated LFM preambles in parallel. The cell ID is detected when the output of a correlator is the largest among the outputs of the parallel LFM correlators and exceeds a threshold value as follows.

$$\hat{b} = \underset{b}{\mathrm{argmax}} |r^{\mathrm{LFM}}|^2 > \gamma \tag{42}$$

When the channel is flat fading, the cross-correlation between the received signal and the locally-generated LFM waveforms for cell ID b is given as follows.

$$\begin{aligned} r^{\mathrm{LFM}} &= \frac{1}{T_{\mathrm{LFM}}}\int_0^{T_{\mathrm{LFM}}} y(s+t)\left(x^{\mathrm{LFM}}(s)\right)^* ds \\ &= \eta h R^{\mathrm{LFM}}(t, f_D) + \tilde{w}^{\mathrm{LFM}} \end{aligned} \tag{43}$$

Then, the detection probability of the correct cell ID is obtained as shown below.

$$P^{\mathrm{LFM}}_{\mathrm{D},t=0} = \frac{1}{2} Q_1\left(\frac{\sqrt{\lambda^{\mathrm{LFM}}}}{\sigma^{\mathrm{LFM}}}, \frac{2\sqrt{\gamma}}{\sigma^{\mathrm{LFM}}}\right) e^{\frac{\lambda^{\mathrm{LFM}}}{2\left(\sigma^{\mathrm{LFM}}\right)^2}} \sum_{i=0}^{B} (-1)^i \hat{C}_i^B \tag{44}$$

The non-centric parameter, λ^{LFM}, is given as follows.

$$\begin{aligned} \lambda^{\mathrm{LFM}} = \eta^2 &\left(Re\left\{hR^{\mathrm{LFM}}(t, f_D)\right\}\right)^2 \\ &+ \eta^2\left(Im\left\{hR^{\mathrm{LFM}}(t, f_D)\right\}\right)^2 \end{aligned} \tag{45}$$

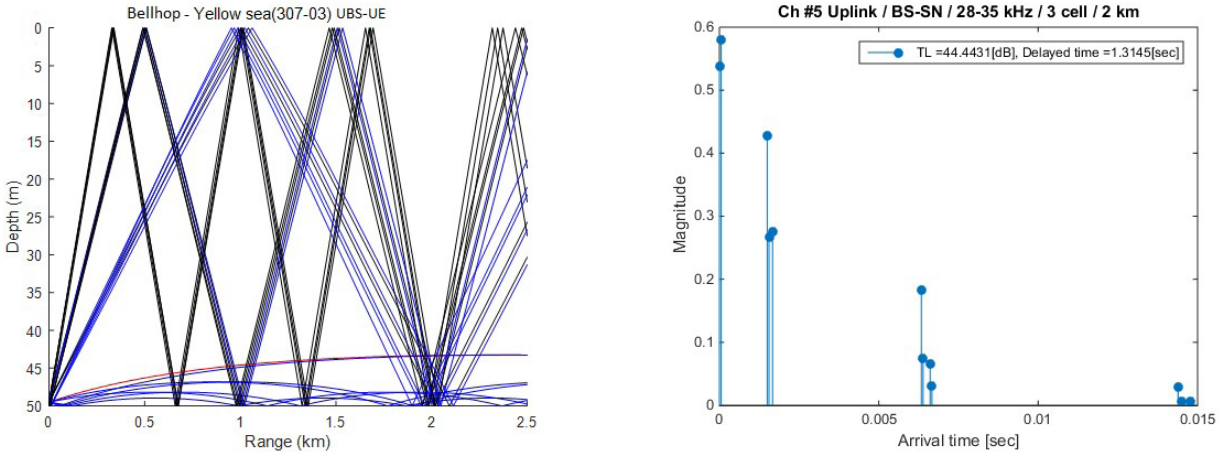

(a) Eigen Ray

(b) Power delay profile

FIGURE 9. Bellhop channel model used in the simulation.

The false alarm probability in the LFM-CST is given as follows.

$$P_{\mathrm{FA}}^{\mathrm{LFM}} = 1 - P_{\mathrm{D},t=0}^{\mathrm{LFM}} \tag{46}$$

In addition, the coarse timing corresponding to the cell ID b is obtained jointly with the cell ID as follows.

$$t_{acq}^{\hat{b}}(t) = \left\{ t : |r^{\mathrm{LFM}}(t)|^2 > \gamma \right\} \tag{47}$$

IV. SIMULATION RESULTS

In this section, the performance of two proposed cell search techniques (ZCS-CST and LFM-CST) for UAC systems is evaluated by simulation. The 3-cell model discussed in Section II is used for the simulation. As shown in Fig. 1, one UE is located at the boundary of the cell 1 ($x_0 = 4.5$ km and $y_0 = 0.15$ km). Thus, UBS 1 should be detected as a serving cell for the UE, while UBS2 and UBS3 are regarded as interfering cells. The cell radius R_c is set to 5 km. The simulation model can be considered as an asynchronous system because there is a large discrepancy in the TDoA owing to the low speed of the sound wave. In addition, the downlink frame structure shown in Fig. 2 is used for preamble detection, synchronization, cell searching, and data transmission. Simulation parameters for both CSTs are summarized in Table 1. For the ZCS-CST, an LFM preamble, which is common to all UBs, is generated by (5) using the fixed ω value of 4 kHz. For the LFM-CST, multiple LFM preambles are generated by (13) using three different ω_b values of 3 kHz, 3.5 kHz, and 4 kHz for UBS1, UBS2, and UBS3, respectively. Different values of ω_b are chosen such that the cross-correlation value between the LFM preambles is small. For the ZCS-CST, three ZCS-2 are generated by (6) with the cell IDs, $u_b = \{6, 7, 8\}$, for 3 UBSs. ZCS-2 carrying the cell ID information is generated with a prime sequence length of $N_{\mathrm{ZC}} = 241$. For the LFM-CST, ZCS-2 is generated using a root index of 5, which is common for all UBSs.

TABLE 1. Simulation parameters.

Parameters	Values
Channel bandwidth	5 kHz
Subcarrier spacing	9.76 Hz
Carrier frequency	24.5 kHz
Symbol duration	0.125 sec
SNR [dB]	10
Number of UBSs	3

In the simulation, two different channels are used: AWGN and multipath channels. The AWGN channel is used to verify the analytic results derived in this study. The multipath channel is used to evaluate the performance of the proposed technique in underwater acoustic channels [36]–[40]. The multipath channel considered in this study is generated by the Bellhop channel simulator, widely used for underwater acoustic communication. The parameters for the Bellhop channel simulator are set with the given information in the field experimental site (distance: 2 km, depth: 50 m). Fig. 9 shows the multipath channel and power delay profile generated by the simulator. In Table 2, the power delay profile consisting of 12 paths, each experiencing Rician fading with a different k factor, is listed with the corresponding path delay and magnitude. A Doppler shift is applied to the LOS (f_{dLOS}) and (f_{dNLOS}) components, creating a time-varying channel.

Fig. 10 shows the detection and false alarm probabilities of the ZCS-CST and LFM-CST in the AWGN channel. In the ZCS-CST, the cell search operation is performed with the parallel ZCS correlators only when the preamble is successfully detected with a single LFM correlator. The analytical results for the detection probability is obtained in (40) by multiplying the preamble detection probability and CID detection probability. The computation of the Marcum function in (33) is numerically performed by a MATLAB built-in function. For the simulation, the SNR is set to -10 dB. From Fig. 10(a), the simulation result ($f_d = 0$ Hz) agrees well with the

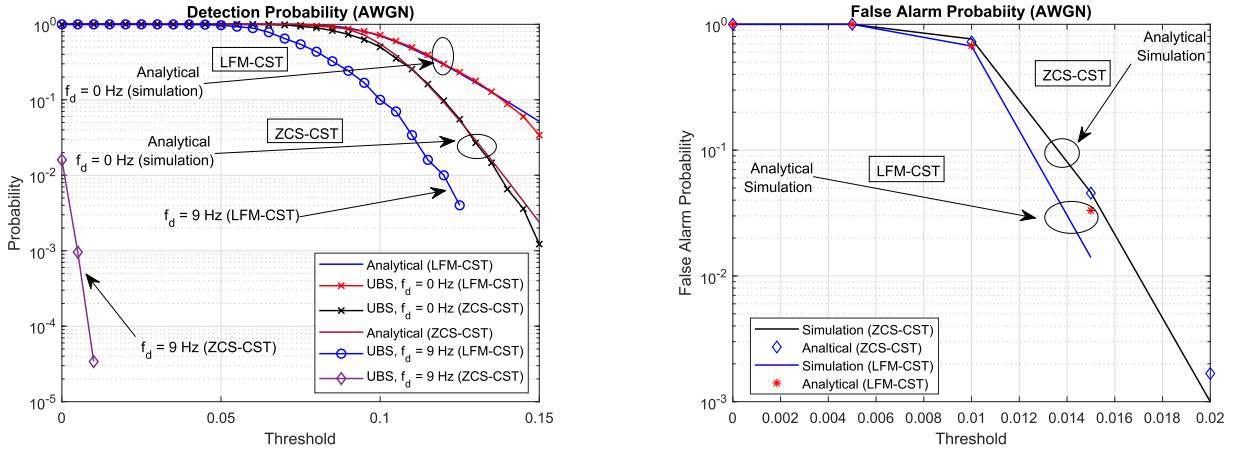

(a) Detection probability (b) False alarm probability

FIGURE 10. Detection and false alarm probabilities of LFM-CST and ZCS-CST in the AWGN channel.

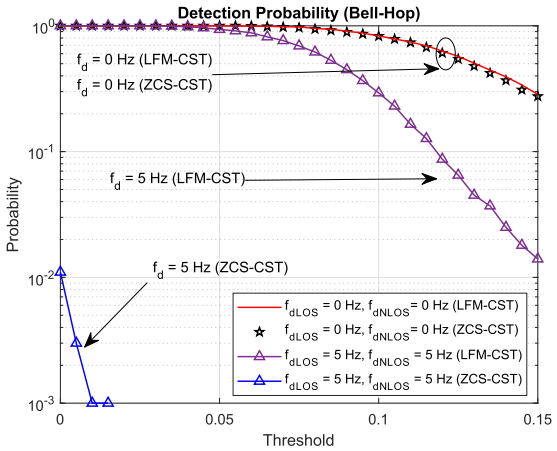

FIGURE 11. Detection probabilities of the ZCS-CST and LFM-CST in the time-varying multipath channel (Bellhop channel).

analytical result in (40). The cell ID can be estimated with a high detection probability when there is no Doppler shift. When the Doppler shift is 9 Hz, the preamble is detected correctly; however, the LFM correlator produces a timing error. The Doppler shift causes the correlation value to drop to almost zero, resulting in failure of the cell ID estimation. In the LFM-CST, the preamble detection and cell ID detection are performed jointly using parallel LFM correlators. As shown in Fig. 10(a), the simulation results ($f_d = 0$ Hz) agree well with the analytical results in (44). The detection probability of the LFM-CST decreases more slowly than that of the ZCS-CST as the Doppler shift increases because the parallel LFM correlators used in the LFM-CST are insensitive to the Doppler shift, whereas the parallel ZCS correlators used in the ZCS-CST are sensitive to the synchronization error. Fig. 10(b) shows the false alarm probability of the ZCS-CST and LFM-CST in the AWGN channel. From Fig. 10(b), it can be seen that the simulation result agrees well with the analytical result in (41) and (46).

TABLE 2. Power delay profile generated by the Bellhop channel model.

Path delay [ms]	Magnitude	K factor
0	0.537	43.50
0.06	0.580	52.48
1.50	0.427	19.95
1.56	0.267	119.31
1.67	0.274	61.68
6.33	0.183	12.59
6.39	0.073	79.43
6.61	0.0650	31.62
6.67	0.0303	50.12
14.39	0.0289	50.12
14.50	0.0065	31.62
14.78	0.0067	12.59

Fig. 11 shows the detection probabilities of the ZCS-CST and LFM-CST in the multipath channels generated by the Bellhop channel simulator. From this figure, it can be seen that the detection probabilities of the ZCS-CST and LFM-CST are similar when there is no Doppler shift ($f_{dLOS} = 0, f_{dNLOS} = 0$). In the presence of the Doppler shift ($f_{dLOS} = f_{dNLOS} = 5Hz$) or $\epsilon = 0.5$, the detection probability of the correct CID in the ZCS-CST decreases significantly. However, the performance degradation in the LFM-CST is not significant.

Table 3 lists the computational complexity required for the cell search in terms of the number of complex multiplications. Here, it is assumed that an AUV is moving at a velocity of 7.71 m/s, the maximum speed attained by an AUV, in an underwater environment [41]. The movement of the AUV will create a maximum Doppler shift of 128 Hz, resulting in a shift of the peak position by 20 samples in the preamble detector (LFM correlator). Thus, the value of the tolerance timing (ζ) is set to 20 samples in the ZCS-CST. In addition, B is set to 20. Here, N_s denotes the number of samples.

V. EXPERIMENTAL RESULTS

A new research project on the development of an underwater cellular system with a period of 7 years (2015-2021)

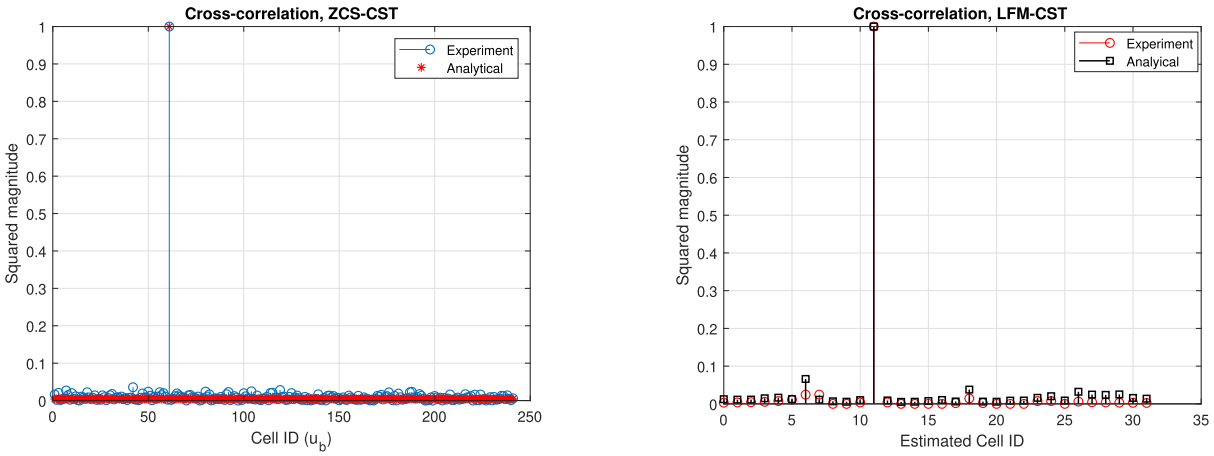

(a) ZCS-CST (b) LFM-CST

FIGURE 12. Cross-correlation properties of the ZCS-CST and LFM-CST: experiment vs. analytical.

TABLE 3. Complexity comparison of the cell search techniques.

CST	Number of complex multiplications	Example
ZCS-CST	$(N_{LFM} \times N_s)+$ $(N_{ZC} \times N_s) \times \zeta$	$(1 \times 625)+$ $(20 \times 512) \times 20$ =2,054,25
LFM-CST	$(N_{LFM} \times N_s)+$ $(N_{ZC} \times N_s)$	$(20 \times 625)+$ (1×512) =1,3012

TABLE 4. Detection probabilities of the ZCS-CST and LFM-CST: Experiment.

Cell search technique	ZCS-CST	LFM-CST
Cell ID	u_b=61	$\beta_b, f_b = 0.5kHz, -0.5kHz$
Number of trials	282	282
Number of successes	277	282
Number of failures	05	00
Success rate [%]	98.2	100

was launched in Korea. Its final goal was to deploy an underwater cellular system connected to a terrestrial cellular network (LTE). The project consisted of two phases: the development of the underwater cellular system and network interworking (the terrestrial cellular network and underwater cellular network). For the development of the underwater cellular system, a field experiment was performed in the sea of the Korean peninsula. Although various transmission/multiplexing schemes (OFDM, CDMA, and chirp spread spectrum (CSS)) were considered, an OFDM-based cellular system was developed in this study. For the OFDM parameters, the carrier frequency, bandwidth, subcarrier spacing, and FFT size were set to 12 kHz, 5 kHz, 9.765 Hz, and 512, respectively. The number of used subcarriers and the effective bandwidth were 498 and 4.863 kHz, respectively. The OFDM symbol length, CP length, and sampling rate were 125 ms, 22.6 ms, and 5 kHz, respectively. The transmit power was set to 28 Watts. In addition, the downlink frame structure shown in Fig. 2 was used for signal detection, synchronization, cell searching, and data transmission. The noise power was estimated from the received signal by measuring the power in the zero-padding zone at the tail of the frame. In the experiment, the DP and SSs used for signal detection, synchronization, and cell searching were generated by a signal generator. The amplifier, transducer, analog filter, digital filter, hydrophone, ADC/DAC, and Zynq-7100 Chipset board developed for the experiment were used to acquire data. In this experiment, the boats connected to the transmitter and receiver were anchored.

For the ZCS-CST, an LFM waveform was generated by (5) with $\omega = 4$ kHz. ZCS-2 was generated by (6) with a root index $u_b = 61$ in the transmitter side (UBS). In the receiver side (UE), the received signal was first correlated with a locally-generated LFM waveform to detect the preamble and coarse timing. Based on the reference timing obtained by the preamble detector, the received ZCS-2 was correlated with the locally-generated 241 ZCS sequences in parallel to estimate the cell ID. For the LFM-CST, the cell ID in the transmitter side (UBS) was mapped with $\omega = -0.5$ kHz and $f_b = 0.5$ kHz, as given in (13). ZCS-2 was generated by (6) with a root index of 11. In the receiver side (UE), the received signal was correlated with the locally-generated 32 LFM waveforms in parallel to estimate the coarse timing and cell ID.

Fig. 12 shows the cross-correlation properties of the two proposed sequences using the data set obtained from the experiment. From Fig. 12(a) and (b), the experiment results of ZCS-CST and LFM-CST agreed well with the analytical results given in (12) and (15), respectively. The experiment was repeated 282 times at different times to obtain the probability of correct cell ID detection. As listed in Table 4, the success rates of both techniques for the correct cell ID were higher than 98%. The success rate of the ZCS-CST was also

high because the boats were anchored. In this experiment, the UBS and UE were dropped from each boat and placed on the bottom of water. The data acquisition was made through the cables made through the cables (connecting node with boat) on the boats. However, if the experiment was conducted in a moving environment, the detection probability of ZCS-CST would decrease significantly owing to its sensitivity to the Doppler shift.

VI. CONCLUSION

In this paper, two different types of cell search techniques (ZCS-CST and LFM-CST) for underwater cellular systems were proposed to detect the identity of the UBS at the physical layer. In the ZCS-CST, parallel ZCS correlators were used in the receiver (UE) to detect the cell ID (UBS), which was mapped to the root index of the ZCS. In the LFM-CST, parallel LFM correlators were used in the receiver to detect the cell ID (UBS), which was mapped to the parameters of the LFM waveform. Based on the simulation and experiment, both techniques achieved a high detection probability in the AWGN and multipath channels when there was no Doppler shift. However, from the simulation, the detection probability of the ZCS-CST was shown to decrease significantly in the AWGN and multipath channels when the Doppler shift was present. The performance degradation of the LFM-CST was not significant in both channels when the Doppler shift was present. Thus, the ZCS-CST or LFM-CST could be used for fixed underwater cellular systems, where sensor nodes or UEs are anchored. However, the LFM-CST would be beneficial for mobile underwater cellular systems, where mobile UEs, such as AUVs and sea gliders, are used.

REFERENCES

[1] S. Sendra, J. Lloret, J. M. Jimenez, and L. Parra, "Underwater acoustic modems," *IEEE Sensors J.*, vol. 16, no. 11, pp. 4063–4071, Jun. 2016.
[2] X. Yu, X. Zhuang, X. Li, and Y. Zhang, "Real-time observation of range-averaged temperature by high-frequency underwater acoustic thermometry," *IEEE Access*, vol. 7, pp. 17975–17980, 2019.
[3] J. Qiu, Z. Xing, C. Zhu, K. Lu, J. He, Y. Sun, and L. Yin, "Centralized fusion based on interacting multiple model and adaptive Kalman filter for target tracking in underwater acoustic sensor networks," *IEEE Access*, vol. 7, pp. 25948–25958, 2019.
[4] M. Erol-Kantarci, H. T. Mouftah, and S. Oktug, "A survey of architectures and localization techniques for underwater acoustic sensor networks," *IEEE Commun. Surveys Tuts.*, vol. 13, no. 3, pp. 487–502, 3rd Quart., 2011.
[5] H.-P. Tan, R. Diamant, W. K. G. Seah, and M. Waldmeyer, "A survey of techniques and challenges in underwater localization," *Ocean Eng.*, vol. 38, nos. 14–15, pp. 1663–1676, Oct. 2011.
[6] I. F. Akyildiz, D. Pompili, and T. Melodia, "Underwater acoustic sensor networks: Research challenges," *Ad Hoc Netw.*, vol. 3, no. 3, pp. 257–259, 2005.
[7] A. Gkikopouli, G. Nikolakopoulos, and S. Manesis, "A survey on underwater wireless sensor networks and applications," in *Proc. 20th Medit. Conf. Control Autom. (MED)*, Barcelona, Spain, Jul. 2012, pp. 1147–1154.
[8] M. Chitre, S. Shahabudeen, and M. Stojanovic, "Underwater acoustic communications and networking: Recent advances and future challenges," *Marine Technol. Soc. J.*, vol. 42, no. 1, pp. 103–116, 2008.
[9] J. Li, Y. V. Zakharov, and B. Henson, "Multibranch autocorrelation method for Doppler estimation in underwater acoustic channels," *IEEE J. Ocean. Eng.*, vol. 43, no. 4, pp. 1099–1113, Oct. 2018.
[10] J. Li and Y. V. Zakharov, "Efficient use of space-time clustering for underwater acoustic communications," *IEEE J. Ocean. Eng.*, vol. 43, no. 1, pp. 173–183, Jan. 2018.
[11] S. Zhou and Z. Wang, *OFDM for Underwater Acoustic Communications*. New York, NY, USA: Wiley, 2014.
[12] Y. S. Cho, J. Kim, W. Y. Yang, and C. G. Kang, *MIMO-OFDM Wireless Communications With MATLAB*. Singapore: Wiley, 2010.
[13] B. Li, S. Zhou, M. Stojanovic, L. Freitag, and P. Willett, "Multicarrier communication over underwater acoustic channels with nonuniform Doppler shifts," *IEEE J. Ocean. Eng.*, vol. 33, no. 2, pp. 198–209, Apr. 2008.
[14] Z. Tang, R. C. Cannizzaro, G. Leus, and P. Banelli, "Pilot-assisted time-varying channel estimation for OFDM systems," *IEEE Trans. Signal Process.*, vol. 55, no. 5, pp. 2226–2238, May 2007.
[15] T. Zemen and C. F. Mecklenbrauker, "Time-variant channel estimation using discrete prolate spheroidal sequences," *IEEE Trans. Signal Process.*, vol. 53, no. 9, pp. 3597–3607, Sep. 2005.
[16] T. T. Cai and L. Wang, "Orthogonal matching pursuit for sparse signal recovery with noise," *IEEE Trans. Inf. Theory*, vol. 57, no. 7, pp. 4680–4688, Jul. 2011.
[17] J. Wu and P. Fan, "A survey on high mobility wireless communications: Challenges, opportunities and solutions," *IEEE Access*, vol. 4, pp. 450–476, 2016.
[18] W. Li, S. Zhou, P. Willett, and Q. Zhang, "Preamble detection for underwater acoustic communications based on sparse channel identification," *IEEE J. Ocean. Eng.*, vol. 44, no. 1, pp. 256–268, Jan. 2019.
[19] B. S. Sharif, J. Neasham, O. R. Hinton, and A. E. Adams, "A computationally efficient Doppler compensation system for underwater acoustic communications," *IEEE J. Ocean. Eng.*, vol. 25, no. 1, pp. 52–61, Jan. 2000.
[20] S. F. Mason, C. R. Berger, S. Zhou, and P. Willett, "Detection, synchronization, and Doppler scale estimation with multicarrier waveforms in underwater acoustic communication," *IEEE J. Sel. Areas Commun.*, vol. 26, no. 9, pp. 1638–1649, Dec. 2008.
[21] T. M. Schmidl and D. C. Cox, "Robust frequency and timing synchronization for OFDM," *IEEE Trans. Commun.*, vol. 45, no. 12, pp. 1613–1621, Dec. 1997.
[22] M. Stojanovic, "Design and capacity analysis of cellular-type underwater acoustic networks," *IEEE J. Ocean. Eng.*, vol. 33, no. 2, pp. 171–181, Apr. 2008.
[23] B. Srinivasan and V. Rodoplu, "Capacity of underwater acoustic OFDM cellular networks," in *Proc. IEEE OCEANS*, Sydney, NSW, Australia, no. 1, May 2010, pp. 1–10.
[24] T. C. Yang, "Code division multiple access based multiuser underwater acoustic cellular network," *J. Acoust. Soc. Amer.*, vol. 130, no. 4, p. 2347, 2011.
[25] F. Akhoundi, J. A. Salehi, and A. Tashakori, "Cellular underwater wireless optical CDMA network: Performance analysis and implementation concepts," *IEEE Trans. Commun.*, vol. 63, no. 3, pp. 882–891, Mar. 2015.
[26] F. Akhoundi, M. V. Jamali, N. B. Hassan, H. Beyranvand, A. Minoofar, and J. A. Salehi, "Cellular underwater wireless optical CDMA network: Potentials and challenges," *IEEE Access*, vol. 4, pp. 4254–4268, 2016.
[27] S. Sesia, I. Toufik, and M. Baker, *LTE—The UMTS Long Term Evolution: From Theory to Practice*. Chichester, U.K.: Wiley, 2011.
[28] *Evolved Universal Terrestrial Radio Access (E-UTRA); Physical Channels and Modulation (Release 12)*, document 3GPP TS 36.211 V 12.3.0, Oct. 2014
[29] R. Pec, M. S. Khan, M. Asim, and Y. S. Cho, "Random access for underwater acoustic cellular systems," *Sensors*, vol. 18, no. 2, p. 432, 2018.
[30] M. Stojanovic and J. Preisig, "Underwater acoustic communication channels: Propagation models and statistical characterization," *IEEE Commun. Mag.*, vol. 47, no. 1, pp. 84–89, Jan. 2009.
[31] S. Beyme and C. Leung, "Efficient computation of DFT of Zadoff-Chu sequences," *Electron. Lett.*, vol. 45, no. 9, pp. 461–463, Apr. 2009.
[32] B. C. Berndt, R. Evans, and K. Williams, *Gauss and Jacobi Sums*. New York, NY, USA: Wiley, 1998.
[33] A. Jeffrey and D. Zwillinger, *Table of Integrals, Series and Products*. Amsterdam, The Netherlands: Elsevier, 2000.
[34] M. K. Song and V. K. Bhargava, "Performance analysis of cell search in W-CDMA systems over Rayleigh fading channels," *IEEE Trans. Veh. Technol.*, vol. 51, no. 4, pp. 749–759, Jul. 2002.
[35] A. Nuttall, "Some integrals involving the Q_M function," *IEEE Trans. Inf. Theory*, vol. 21, no. 1, pp. 95–96, Jan. 1975.
[36] R. J. Urick, *Principles of Underwater Sound*. New York, NY, USA: McGraw-Hill, 1983.
[37] E. M. Sozer, M. Stojanovic, and J. G. Proakis, "Design and simulation of an underwater acoustic local area network," in *Proc. OpenNetwork*, Washington, DC, USA, Aug. 1999, pp. 1–5.

[38] J. Catipovic, A. Baggeroer, K. Von Der Heydt, and D. Koelsch, "Design and performance analysis of a digital acoustic telemetry system for the short range underwater channel," *IEEE J. Ocean. Eng.*, vol. 9, no. 4, pp. 242–252, Oct. 1984.
[39] R. Galvin and R. F. W. Coates, "Analysis of the performance of an underwater acoustic communications system and comparison with a stochastic model," in *Proc. OCEANS*, Brest, France, Sep. 1994, pp. III-478–III-482.
[40] X. Geng and A. Zielinski, "An eigenpath underwater acoustic communication channel model," in *Proc. OCEANS MTS/IEEE*, San Diego, CA, USA, Oct. 1995, pp. 1189–1196.
[41] H. N. Arafat, D. J. Stilwell, and W. L. Neu, "Development of a dynamic model of a small high-speed autonomous underwater vehicle," in *Proc. IEEE OCEANS*, Boston, MA, USA, Sep. 2006, pp. 1–6.

MUHAMMAD ASIM was born in Sialkot, Punjab, Pakistan, in 1989. He received the B.S. degree in electronics engineering from COMSATS University, Khyber Pakhtunkhwa, Pakistan, in 2013, and the M.S. degree in electrical and electronics engineering from Chung-Ang University, Seoul, South Korea, in 2019, where he is currently pursuing the Ph.D. degree in electrical and electronics engineering. From 2013 to 2017, he was with Pak German Engineers (PGE) as an Engineer. Since 2017, he has been a Research Assistant with the Mobile Communications Laboratory, Chung-Ang University. His research interests include areas of underwater wireless communication systems, OFDM, digital signal processing, and LPWAN.

ROTHNA PEC was born in Pursat, Cambodia, in 1988. He received the B.S. from the Institute of Technology of Cambodia (ITC), Cambodia, in 2011, and the M.S. and Ph.D. degrees from Chung-Ang University, Seoul, South Korea, in 2013 and 2017, respectively, all in electrical and electronics engineering.

From 2011 to 2018, he was a Research Assistant with the Mobile Communications Laboratory, Chung-Ang University. Since 2018, he has been a Lecturer and a Researcher with ITC. His research interests include beamforming, synchronization, and 5G.

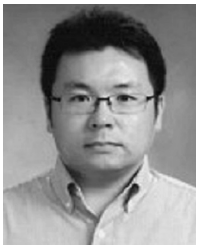

TAE HO IM was born in South Korea. He received the B.S., M.S., and Ph.D. degrees in electrical and electronics engineering from Chung-Ang University, Seoul, South Korea, in 2006, 2008, and 2012, respectively. From 2012 to 2014, he was with Samsung Electronics as a Senior Research Engineer, where he was in charge of research and development on the baseband systems for 5G communication systems. In March 2015, he joined the Faculty of Oceanic IT Engineering, Hoseo University. His current research interests include underwater acoustic communications, 5G, and LPWAN.

YONG SOO CHO was born in South Korea. He received the B.S. degree in electronics engineering from Chung-Ang University, Seoul, South Korea, in 1984, the M.S. degree in electronics engineering from Yonsei University, Seoul, in 1987, and the Ph.D. degree in electrical and computer engineering from The University of Texas at Austin, Austin, TX, USA, in 1991. In 1984, he was a Research Engineer with Goldstar Electrical Company, Osan, South Korea. In 2001, he was a Visiting Research Fellow with the Electronics and Telecommunications Research Institute (ETRI). Since 1992, he has been a Professor with the School of Electrical and Electronics Engineering, Chung-Ang University. He has authored 12 books and more than 400 conference articles and holds more than 120 patents. His research interests include the area of mobile communication and digital signal processing, especially for MIMO-OFDM and 5G. He served as the President of the Korean Institute of Communications and Information Sciences, in 2016, and was a recipient of the Dr. Irwin Jacobs Award, in 2013.